ResearchGate

See discussions, stats, and author profiles for this publication at: https://www.researchgate.net/publication/373422441

Highly Efficient Adsorption of Aqueous Iodine on Polythiophene/α-Manganese dioxide Nanocomposites

Article · August 2023

DOI: 10.1016/j.colsuc.2023.100017

CITATIONS
0

READS
19

4 authors, including:

Aakash Waghmare
Dr. Harisingh Gour University
5 PUBLICATIONS **2** CITATIONS
SEE PROFILE

Roshni Rathore
Dr. Harisingh Gour Vishwavidyalaya Sagar
6 PUBLICATIONS **3** CITATIONS
SEE PROFILE

Archna Pandey
Dr. Harisingh Gour University
52 PUBLICATIONS **323** CITATIONS
SEE PROFILE

All content following this page was uploaded by Aakash Waghmare on 19 October 2023.

The user has requested enhancement of the downloaded file.

Colloids and Surfaces C: Environmental Aspects 1 (2023) 100017

Contents lists available at ScienceDirect

Colloids and Surfaces C: Environmental Aspects

journal homepage: www.journals.elsevier.com/colloids-and-surfaces-c-environmental-aspects

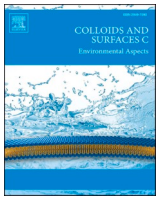

Highly efficient adsorption of aqueous iodine on polythiophene/α-manganese dioxide nanocomposites

Aakash Waghmare [a], Roshni Rathore [a], Archna Pandey [a], Vimlesh Chandra [a,b,*]

[a] Department of Chemistry, Dr. Harisingh Gour University, Sagar, M.P. 470003, India
[b] School of Applied Material Sciences, Central University of Gujarat, Gandhinagar, GJ 382030, India

ARTICLE INFO

Keywords:
Adsorption
Nanocomposite
Iodine
Water
Recyclability

ABSTRACT

The discharge of wastewater containing toxic and radioactive iodine into water leads to a negative impact on aquatic life, animals and humans. In this work, we synthesized Polythiophene (PTh) and Polythiophene/α-MnO_2 nanocomposite (PTh/α-MnO_2) by the chemical route and used them to remove iodine from aqueous solution. The surface morphology showed presence of rod-shaped α-MnO_2 with a size of 25–200 nm embedded in polythiophene. The interplaner distance was found to be 0.7 nm corresponds to the (211) plane. Specific surface area of PTh and PTh/α-MnO_2 nanocomposite was found to be 22.15 m^2/g and 51.98 m^2/g respectively and equilibrium I_2 adsorption capacity was found to be (q_e) 266.08 mg/g and 304.21 mg/g respectively. Langmuir isotherm ($R^2 = 0.99$) fitted well compared to Freundlich isotherm ($R^2 = 0.84$) indicates monolayer adsorption of iodine onto adsorbent surface. The adsorbent is stable, recyclable, high adsorption capacity, and environment friendly so it can be used at large scale for treatment of I_2 contaminated water.

1. Introduction

Demand for energy is growing across the world due to the rapid increase in population and industries [1]. Among all the existing energy sources, nuclear energy is a safe and clean source of energy. However, radioactive waste produced during the generation of nuclear energy causes environmental pollution and remains a danger to human health for many years [2]. Chornobyl (Pripyat, Ukraine, 1986) and Fukushima (Okuma, Japan, 2011) nuclear power plant accidents generated various types of radioactive wastes [3,4]. Among those, ^{131}I, and ^{129}I were the main radionuclides spread in the environment, having a half-life of 8 days and 11.57×10^7 years, respectively [5,6]. Radioiodine (^{131}I) is also used to treat hyperthyroidism or thyroid cancer [7]. Radioiodine contaminations are often detected in surface water, seawater, and groundwater due to its solubility in water [1,4]. The World Health Organization (WHO) recommends that the drinking water standards for iodine should be below 0.1 mg/L in both drinking water and groundwater. A recent study conducted by Zhi et al. indicates that approximately 19.8 % of China's land area is classified as a high-risk zone for elevated levels of iodine in groundwater [8]. The radioiodine toxicity poses a serious threat to both human health and the environment during its lengthy decay process [9]. On the other hand, radioactive iodine that has accumulated in the human body's living tissues can result in thyroid cancer, leukemia, and other life-threatening diseases [10]. Therefore it is necessary to remove radioactive iodine from water in a safe, affordable, and environmentally friendly manner. Various techniques have been used to remove iodine from aqueous solutions, including physical, chemical, and biological approaches such as solvent extraction, ion exchange, osmosis, membrane separation, precipitation, and adsorption [11]. Solvent extraction is costly and took prolonged time [12]. The disadvantages associated with ion exchange are high operation cost and ion exchangers are quickly damaged by bacteria, oxidising agent, and temperature [13]. The reverse osmosis installation cost is very high, needs routine filter change and maintenance, process is very slow, remove most of the mineral, and amount of water wasted is quite large [14]. Membrane filtration is effective method for removal of iodine however fouling of membrane and pore blockage are main key weakness of the method [15]. Chemical precipitation is effective method for removal of iodine but the expensive chemical cost and huge sludge generation are major drawback of this method [16].

However, adsorption is a more promising method to remove iodine from aqueous solution due to its high efficiency, superior simplicity, and low cost [5]. Recently, activated carbon [17], layered double hydroxidesm [18], metal oxide [19] Mxene [20], metal-organic frameworks

* Corresponding author at: Department of Chemistry, Dr. Harisingh Gour University, Sagar, M.P. 470003, India.
E-mail addresses: vchandg@gmail.com, v.chandra@cug.ac.in (V. Chandra).

https://doi.org/10.1016/j.colsuc.2023.100017
Received 21 July 2023; Received in revised form 23 August 2023; Accepted 24 August 2023
Available online 26 August 2023
2949-7590/© 2023 Elsevier B.V. All rights reserved.

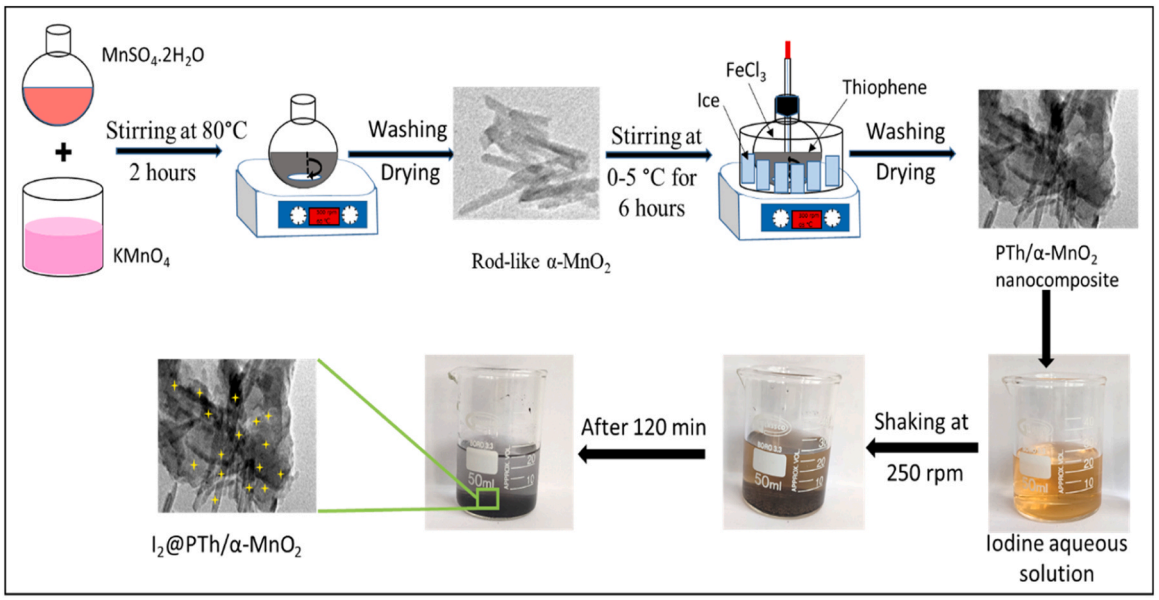

Scheme 1. Preparation of PTh/α-MnO_2 nanocomposite via oxidative polymerization method and iodine adsorption on PTh/α-MnO_2 nanocomposite.

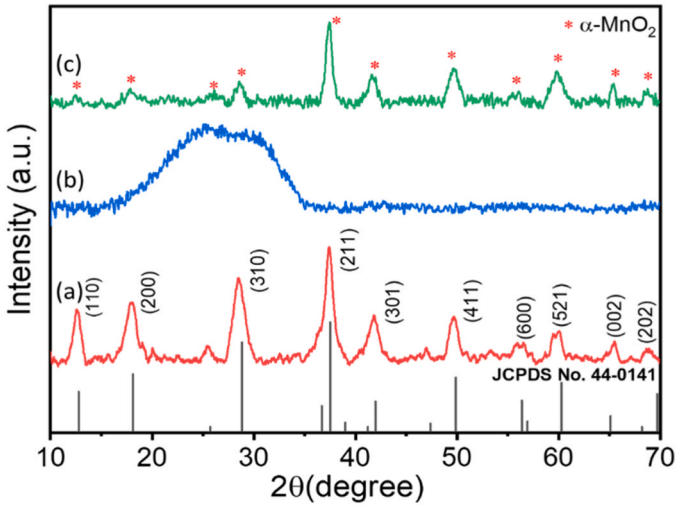

Fig. 1. Powder X-ray diffraction pattern of (a) α-MnO_2, (b) PTh, (c) PTh/α-MnO_2 nanocomposite.

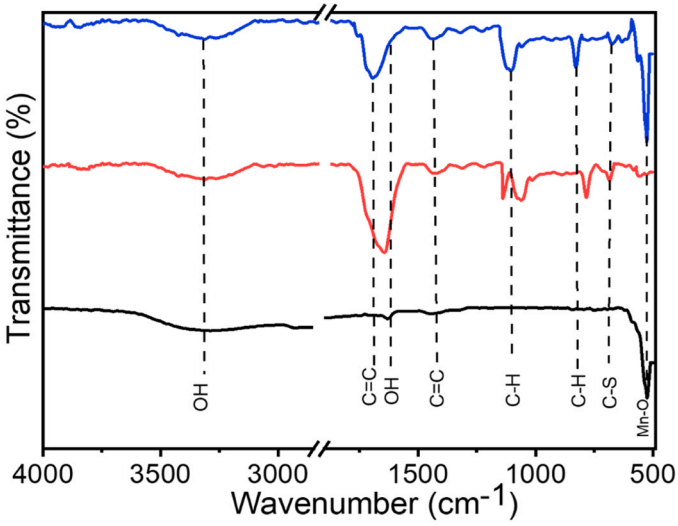

Fig. 2. FTIR spectra of (a) α-MnO_2 (b) PTh (c) PTh/α-MnO_2 nanocomposite.

[21], metal nanoparticles [22], and conducting polymers [23], have been employed for adsorption of radioactive iodine. Metal oxides are potential materials in the field of wastewater treatment because of their high stability, large-scale production at low cost, and environment friendly [24]. In recent years, metal oxides have been widely used in adsorption of iodine, including Cu_2O [25], Ag_2O [7], B_2O_3 [26], Bi_2O_3 [27], Fe_3O_4 [28], and MnO_2 [29]. Among these, MnO_2 has the advantages of easy synthesis, high melting point, diverse morphologies, large surface area, low cost, easy availability, and environmental friendliness [30].

Moreover, conducting polymers are conjugated carbon chains made up of alternating single and double bonds, with highly delocalized and electron-dense π bonds controlling their electrical and optical properties [31]. Conducting polymers such as polyaniline, polypyrrole, and polythiophene have received much research attention for a variety of practical uses, including sensors, photocatalytic activity, and environmental clean-up [32]. Polythiophene is a sulfur-based heterocycle polymer with a free electron lone pair, with appropriate molecular structure, surface area, and a number of interaction sites [33]. Polythiophene has been used in the adsorption of various pollutants like heavy metal [34], nitrobenzene [35], and arsenic [36]. Previous work has reported that modification of polythiophene with metal oxide enhances its surface area, thermal stability, and adsorption capacity [37]. Polythiophene/MnO_2 nanocomposites showed enhanced pseudocapacitive properties [38], photocatalytic degradation efficiency [39], and adsorption capacity [40].

In this paper, we report the synthesis of α-MnO_2, PTh, and PTh/α-MnO_2 nanocomposite via chemical precipitation and oxidative polymerization methods. PTh/α-MnO_2 nanocomposite is environment friendly, low cost, high specific surface area, high adsorption capacity, and better reusability compare to recently reported many adsorbents.

2. Materials and Method

2.1. Chemicals

Manganese sulphate tetrahydrate ($MnSO_4{\cdot}4H_2O$ MW: 169.01 g/mol SRL), Potassium permanganate ($KMnO_4$ MW: 158.03 g/mol Sigma

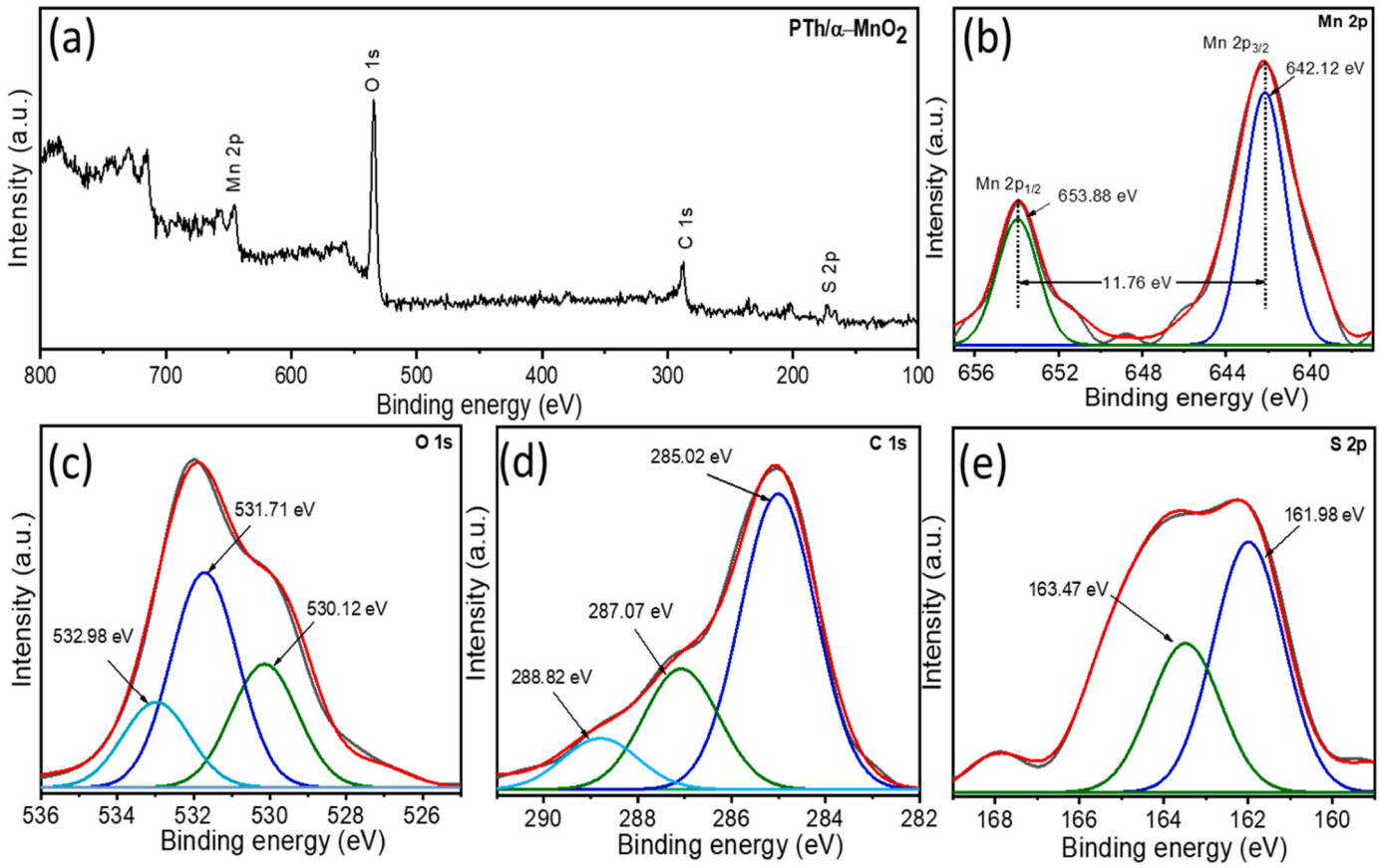

Fig. 3. XPS graphs of PTh/α-MnO_2 nanocomposite (a) Full survey (b) Mn 2p (c) O 1s (d) C 1s (e) S 2p.

Aldrich), Glacial Acetic Acid (CH_3COOH 99 % Merck), Thiophene (C_4H_4S MW: 84.14 g/mol Sigma Aldrich), Iron(III) chloride ($FeCl_3$ MW: 162.20 g/mol Sigma Aldrich), Chloroform ($CHCl_3$ 99 % Loba Chemie), Methanol (CH_3OH 99.5 % Loba Chemie), Hydrochloric acid (HCl 35 % Merck), Sodium hydroxide (NaOH MW:40.00 g/mol Merck), Iodine (I_2 MW:253.8 g/mol Merck) and DI water (H_2O MW:18.02 g/mol Merck).

2.2. Synthesis of rod-like α-MnO_2

The rod-like α-MnO_2 was synthesized using the modified McKenzie co-precipitation method [41]. Firstly, solution-A was prepared by dissolving 3.24 g of $KMnO_4$ in 40 mL of DI water in a 100 mL round bottom flask. The resulting solution-A was heated in a 60 °C for 30 min. Secondly, 1.68 g of $MnSO_4.5\ H_2O$ were dissolved in 50 mL of 2 M solution of CH_3COOH and stirred for 20 min at 60 °C (solution-B). Then mix both solutions under constant stirring at 80 °C for two hours and keep the solution at room temperature. After cooling, the resulting black color precipitate was centrifuged and washed with distilled water and dried at 80 °C for 24 h.

2.3. Synthesis of PTh/α-MnO_2 nanocomposites

PTh/α-MnO_2 nanocomposites were synthesized using the oxidative polymerization method shown in Scheme 1 [42]. First, solution-A was prepared by dispersing the different weights of α-MnO_2 (20, 40, 60, and 80 wt%) and 1 mL thiophene in 50 mL of $CHCl_3$ in a 250 mL round bottom flask and sonicated for 20 min. Then, solution-B was prepared by dissolving 8 g of $FeCl_3$ in 100 mL of $CHCl_3$ and sonicated for 20 min. While maintaining the temperature of solution-A at 0–5 °C, we added solution-B dropwise under continuous stirring. The resulting solution was stirred for 6 h and allowed to polymerize left for 24 h. After polymerization, solution-C was filtered and washed with 200 mL methanol, and the resulting precipitation was resuspended in 100 mL of 1 M HCl and stirred for 2 h. This solution was filtered and washed with double-distilled water until the pH of the precipitation obtained reached 7. Finally, the resulting suspension was dried at 60 °C for 24 h. Synthesis of polythiophene was carried out by the same procedure in the absence of α-MnO_2.

2.4. Characterization

Different instruments were used to investigate the synthesized α-MnO_2, PTh, and PTh/α-MnO_2 nanocomposite samples. The crystallographic structure was obtained using powder X-ray diffraction patterns (Bruker D8 Advance diffractometer) with a Cu K_α irradiation ($\lambda = 1.542$ Å), and the data were collected from 10° to 70° at a scanning rate of 3°/minutes. Functional groups identification was carried out using Fourier transform infrared spectra (Bruker Alfa II) form 500–4000 cm^{-1} with a spectral resolution of 2 cm^{-1}. The surface morphology and element composition were investigated using Scanning electron microscopy (Thermo Scientifc Apreo S) and transmission electron microscopy (G2 30 S-TWIN). The specific surface area, pore volumes, and pore size distribution were found using Brunauer-Emmett-Teller (JWGB Micro 122 W) at a liquid nitrogen temperature (−196 °C). The electronic states of the elements were analyzed using an X-ray photoelectron spectroscopy (PHI 5000 Versa Probe II, FEI Inc) within a range of binding energies from 100 to 800 eV. The concentration of iodine in the aqueous solution was analyzed using UV–Visible Spectrophotometry (Cary 60) in the range of 200–800 nm.

2.5. Iodine adsorption

Firstly, 200 ppm iodine stock solution was prepared by dissolving 200 mg in 1000 mL double-distilled water and storing it in a dark place.

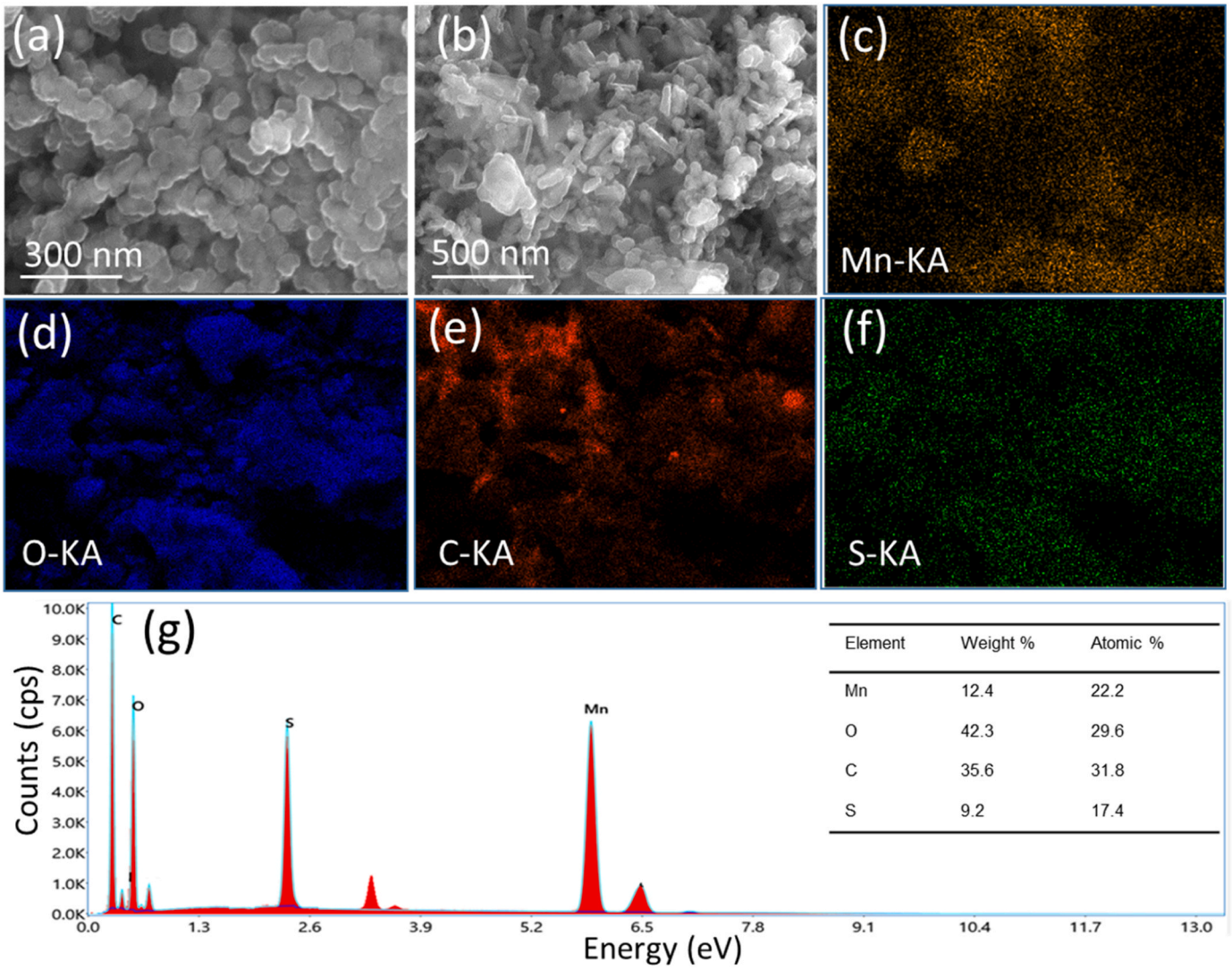

Fig. 4. SEM images (a) PTh (b) PTh/α-MnO_2 nanocomposite (c-f) mapping for Mn, O, C, and S respectively (g) EDAX of PTH/α-MnO_2 nanocomposite.

A batch adsorption experiment was carried out at an initial concentration of 100 ppm, a volume 20 mL, a dose 6 mg, and a contact time 2 h at room temperature. After completion of adsorption process, the filtrate was collected and examined for iodine concentration using a UV/Vis spectrometer at λ_{max} 288 nm [43]. Adsorption capacity and removal efficiency (RE) calculated by the Eqs. (1) and (2).

$$q_e = \frac{(C_0 - C_t) \times V}{W} \quad (1)$$

$$RE\% = \frac{C_0 - C_t}{C_0} \times 100 \quad (2)$$

Where C_0 and C_t (mg/L) are the concentration of iodine solution at initial and at time t, V (mL) is the volume, W is the mass (mg), q_e (mg/g) is the adsorption capacity at equilibrium, and RE% is the percentage removal efficiency.

3. Results and discussion

3.1. Characterization

3.1.1. Powder X-ray diffraction analysis

The powder X-ray diffraction pattern was recorded to examine the phase purity and crystallite size of the synthesized nanomaterials and nanocomposites, as shown in Fig. 1(a–c). The diffraction peaks at 13.0°, 18.1°, 28.9°, 37.6°, 42.2°, 50.1°, 56.4°, 60.2°, 65.6°, 69.3°, and 72.9° corresponds to (110), (200), (310), (211), (301), (411), (600), (521), (002), (541), and (312) crystal planes respectively and are well consistent with α-MnO_2 (JCPDS card no. 44-0141) [44,45]. The XRD pattern of PTh showed a broad peak of 22–35°, indicating its amorphous nature resulting from π-π intermolecular stacking [46]. PTh/α-MnO_2 nanocomposite showed XRD characteristic peaks of α-MnO_2 with decreased intensity. This decrease in the intensity resulted in the presence of amorphous PTh [39]. The Debye-Scherer Eq. (3) was used to calculate the crystallite size of α-MnO_2.

$$D = \frac{k\lambda}{\beta(\cos\theta)} \quad (3)$$

where D (nm) crystallite size, k (0.92) Scherer constant, λ (0.154 nm) wavelength of X-ray for Cu target, β (radians) full width at half maxima, and θ (radians) Bragg angle. The average crystallite size of α-MnO_2 was calculated to be 11.46 nm and 13.06 nm for the bare and composite materials respectively.

3.1.2. FTIR analysis

FTIR spectra were recorded to investigate the functional groups present in α-MnO_2, PTh, and PTh/α-MnO_2 nanocomposite (Fig. 2a–c).

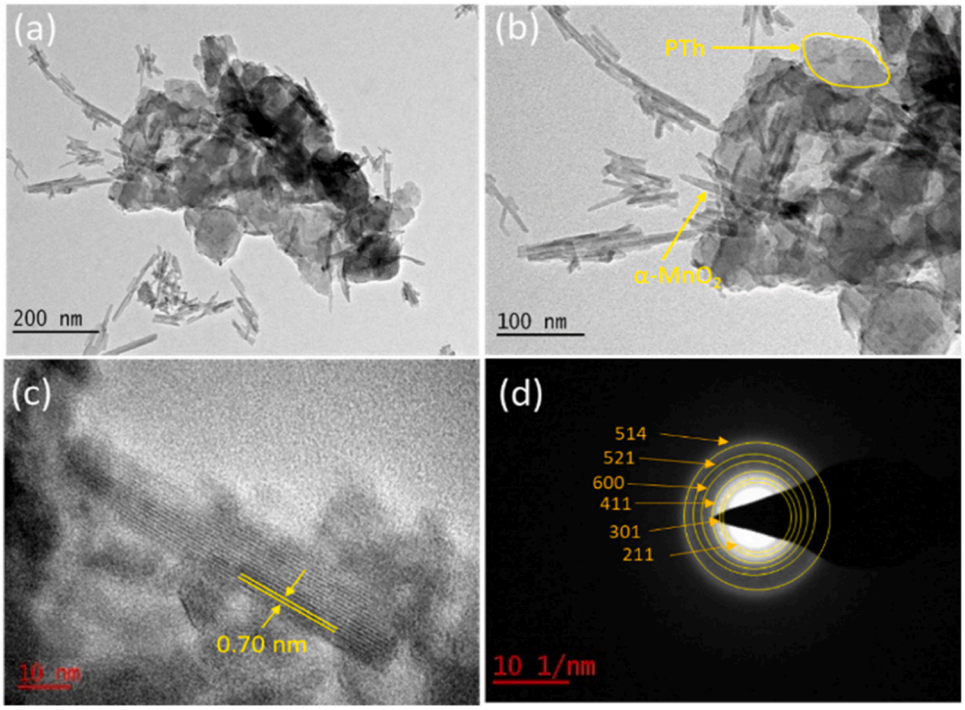

Fig. 5. TEM images (a-b) PTh/α-MnO_2 nanocomposite (c) HR-TEM image of PTh/α-MnO_2 nanocomposite (d) SAED of PTh/α-MnO_2 nanocomposite.

FTIR spectrum of α-MnO_2 showed transmission bands around 3302 cm^{-1} and 1627 cm^{-1} corresponding to bending vibrations of the O-H group. The strong band centered on 529 cm^{-1} corresponds to Mn-O stretching vibration [47]. The spectrum of PTh showed a strong peak at 3440 cm^{-1}, which could be assigned to the stretching vibration band of the OH group. Additionally, there was a band appearance for C═C symmetric stretching vibration at 1435 cm^{-1}, an asymmetric stretching vibration at 1640 cm^{-1}, in-plane deformation vibration of the C−H group at 1079 cm^{-1}, the out-of-plane stretching vibration of the C−H group at 787 cm^{-1}, and the stretching vibration of the C−S group at 685 cm^{-1}[36]. PTh/α-MnO_2 nanocomposite showed bands for α-MnO_2 and PTh. However, the absorbance bands of PTh shifted towards the lower wavenumber in the region 500–1700 cm^{-1}. This shifting mainly comes from the van der waals interaction between PTh and α-MnO_2 [48].

3.1.3. XPS analysis

The XPS spectrum was measured to investigate the chemical states of each element present in the PTh/α-MnO_2 nanocomposite (Fig. 3a–e). The full survey spectrum (Fig. 3a) showed the presence of Mn, O, C, and S elements on the surface of the PTh/α-MnO_2 nanocomposite. The high-resolution XPS spectra of Mn 2p showed two peaks at binding energies of 653.8 eV and 642.12 eV corresponding to the characteristics of Mn $2p_{1/2}$ and Mn $2p_{3/2}$, respectively. The spin-energy separation between Mn $2p_{1/2}$ and Mn $2p_{3/2}$ is 11.72 eV, which agrees well with the previous work [49]. The O 1s spectral peak was deconvoluted into three types of peaks.

The first peak at 533.1 eV belongs to oxygen species weakly adsorbed on a surface in the forms of H_2O, while another two peaks at 531.5 eV and 529.7 eV are attributed to Mn-OH and Mn-O, respectively [50]. The C 1s spectral peak was deconvoluted into three kinds of peaks, the first peak at 288.82 eV belongs to the C═O bond, classical peaks at 287.07 eV and 285.02 eV are attributed to (C−S), and (C−C) [48]. S 2p spectrum was deconvoluted into two peaks. Peaks at 161.98 and 163.47 eV are attributed to S $2p_{1/2}$, and S $2p_{3/2}$, respectively. Peak at 161.98 eV was related to the formation of positively charged sulfur ($S^{\delta+}$), which is generated by the transport of polaron and bipolaron in the polythiophene chain. This finding are in the good agreement with the previous work [36,51,52].

3.1.4. Morphological analysis

SEM images were recorded to investigate the surface morphology of PTh and PTh/α-MnO_2 nanocomposite as shown in Fig. 4a-b. The SEM image of PTh (Fig. 4a) reveals the formation of agglomerated globular morphologies in the PTh polymer matrix [40]. Fig. 4b shows the morphology of the PTh/α-MnO_2 nanocomposite where α-MnO_2 rods are uniformly distributed among PTh polymer globular particles [46,53]. The element mapping showed the presence of C, S, O, and Mn elements homogeneously as shown in Fig. 4c–f. The energy dispersive spectrometry showed the presence of Mn, O, C, and S at atomic percent 12.4 %, 42.3 %, 35.6 %, and 9.2 %, respectively (Fig. 4g). The atomic composition of Mn:O is 1:2 indicated formation of α-MnO_2 phase. The atomic composition of S:C is 1:4 indicating the formation of polythiophene.

Transmission electron microscopy (TEM), high-resolution TEM, and selected area diffraction (SAED) patterns were used to investigate the morphology and crystal structure of the PTh/α-MnO_2 nanocomposite. TEM image of the PTh/MnO_2 nanocomposite (Fig. 5a-b) reveals rod-like α-MnO_2 encapsulated in an agglomerated globular PTh polymeric matrix [54]. The HRTEM image of PTh/α-MnO_2, Fig. 5c, showed lattice fringes with an interplanar distance of 0.70 nm corresponding to (211) lattice plane, indicates the formation of a pure phase [46,55]. The SAED image showed a ring pattern with planes (211), (301), (411), (600), (521), and (514) matching exactly with the X-ray diffraction patterns of α-MnO_2 nanorods [54].

3.1.5. Surface area analysis

The surface area and porosity are essential factors in the adsorption process. Nitrogen adsorption–desorption isotherms were used to investigate the total surface area and porosity of the material. According to the IUPAC classification, the isotherms are of type IV with H3 hysteresis loops as shown in Fig. 6a–c. The BET surface area and pore volumes of α-MnO_2, PTh, PTh/α-MnO_2 nanocomposite were found to be 97.38, 22.15, 51.98 m^2/g, and 0.436, 0.118, 0.259 cm^3/g respectively (Table 1). Specific surface area and pore volumes of a α-MnO_2 drop with

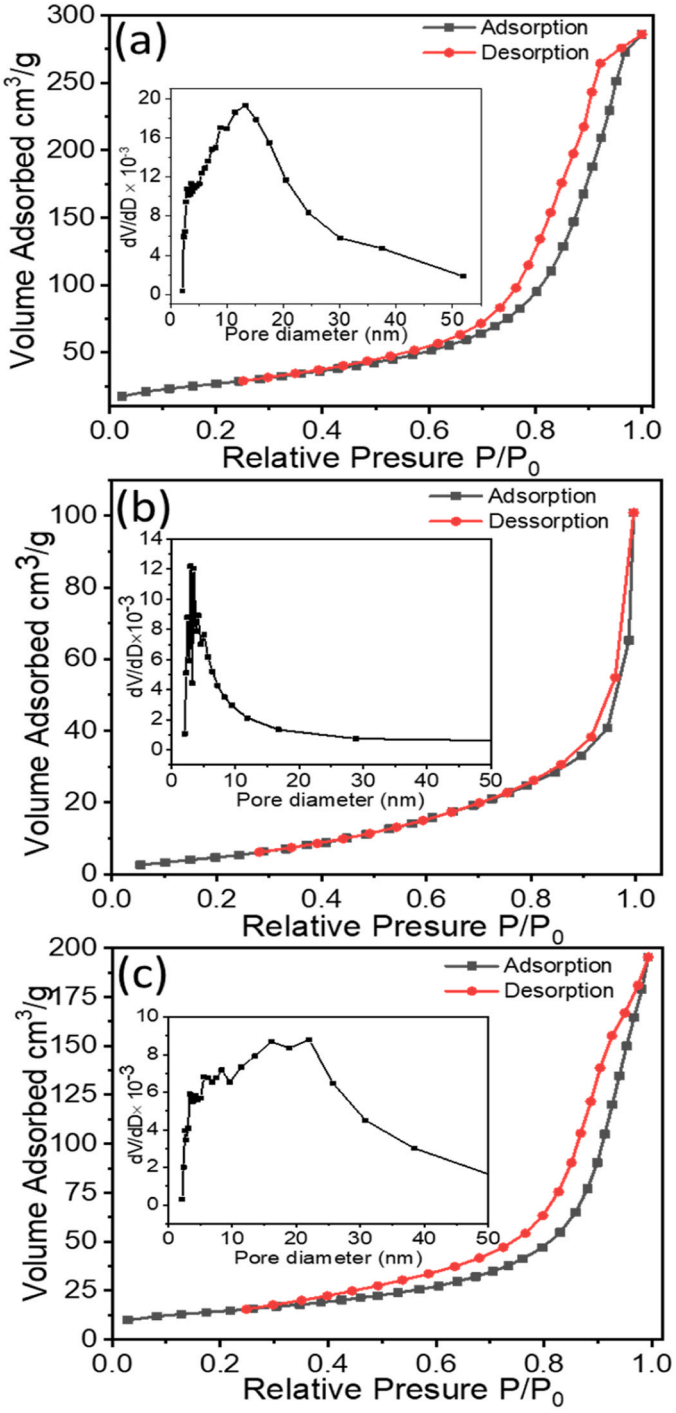

Fig. 6. BET N_2 adsorption–desorption isotherms and Barrett-Joyner-Halenda pore size distribution plots of (a) α-MnO_2, (b) PTh, (c) PTh/α-MnO_2 nanocomposite, respectively.

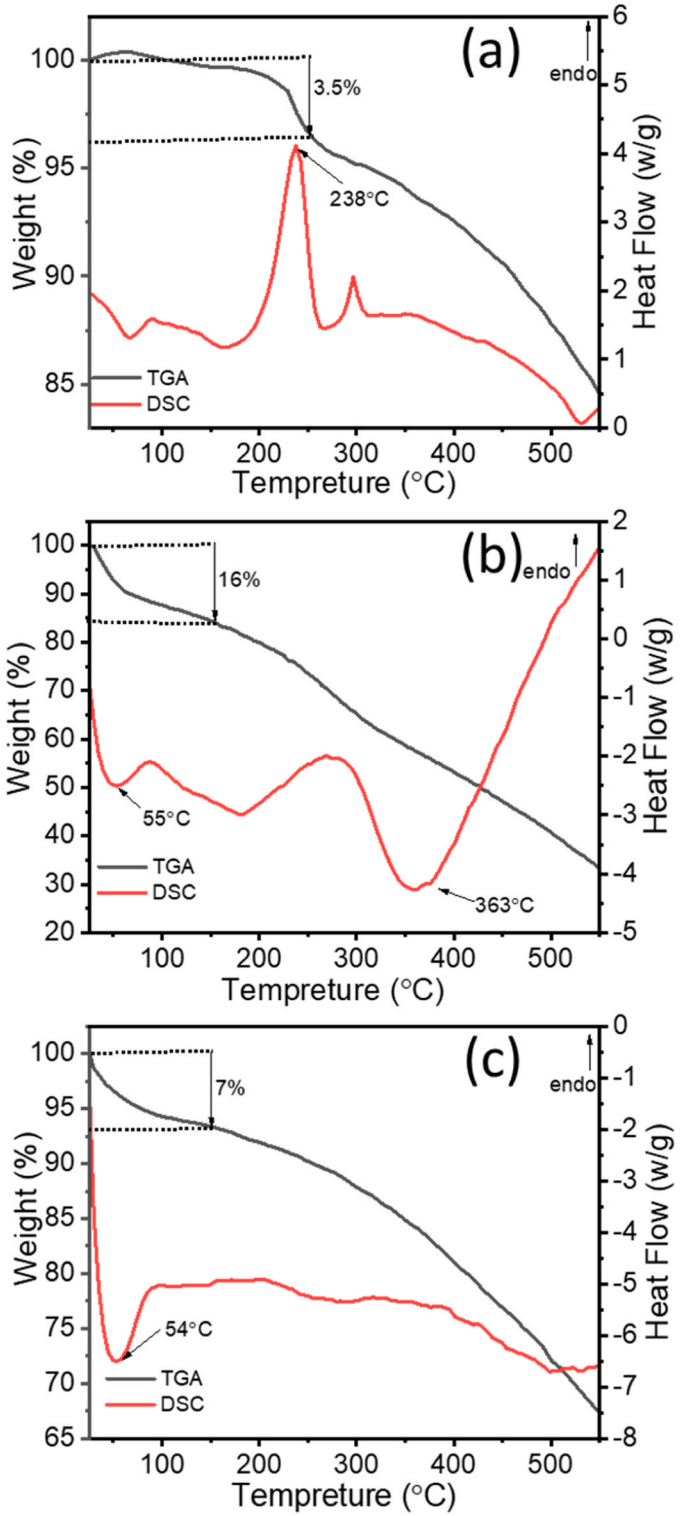

Fig. 7. Thermogravimetric analysis and Differential scanning calorimetry (TGA-DSC) of (a) α-MnO_2, (b) PTh, (c) PTh/α-MnO_2 nanocomposite.

Table 1
The specific surface area, total pore volume, and average pore diameter of α-MnO_2, PTh, and PTh/α-MnO_2 nanocomposite.

Material	Surface area [m^2/g]	Pore volume [cm^2/g]	Pore size [nm]
α-MnO_2	95.38	0.436	17.91
PTh	22.15	0.118	21.34
PTh/α-MnO_2	51.98	0.295	22.71

the increase of the PTh amount because of the blocking of the surface or pores of the composite by the PTh polymer matrix [38]. Based on the Barrett-Joyner-Halenda (BJH) model, materials are classified as microporous, mesoporous, and macroporous if pore sizes < 2 nm, lie between 2 and 50 nm, and > 50 nm in diameter. The pore size of α-MnO_2, PTh, and PTh/α-MnO_2 was found to be 17.91, 21.34, and 22.71 nm, respectively indicating the formation of the mesoporous structure (2–50 nm)

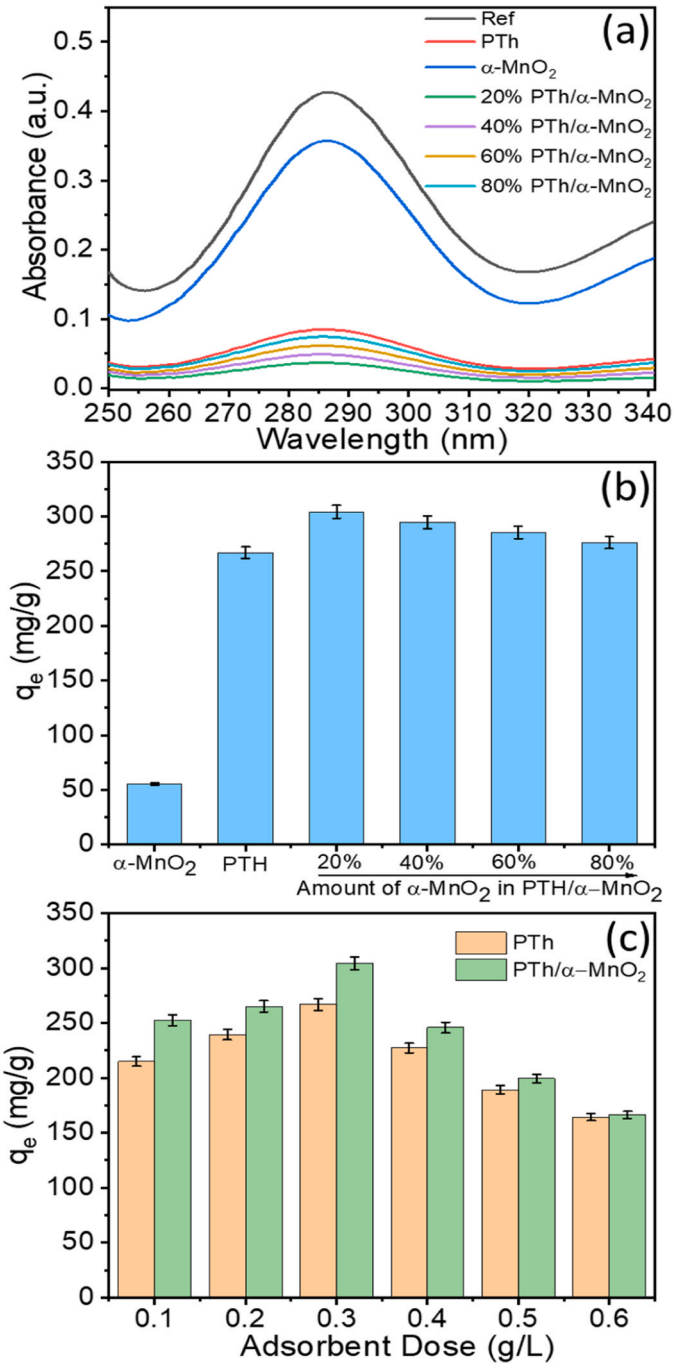

Fig. 8. Effect of different adsorbents (a, b) UV-Vis spectra and adsorption capacity (c) Effect of dose. [Initial I_2 conc. 100 mg/L, dose 0.3 g/L, time 2 h and temperature 25 °C].

[56].

3.1.6. *Thermal analysis*

TGA-DSC measurements were conducted to investigate the microstructure and thermal stability of α-MnO_2, PTh, and the PTh/α-MnO_2 nanocomposite, as shown in Fig. 7a–c. The TGA curve of α-MnO2 exhibited a weight loss of about 3.5 % in the temperature range of 25–250 °C, attributed to the evaporation of weakly bound surface water molecules [57]. An endothermic peak was observed at 238 °C, corresponding to the removal of water molecules [58]. Additionally, as the sample was heated from 250 °C to 550 °C, a 12 % reduction in sample weight occurred, attributed to oxygen loss and the phase transition from

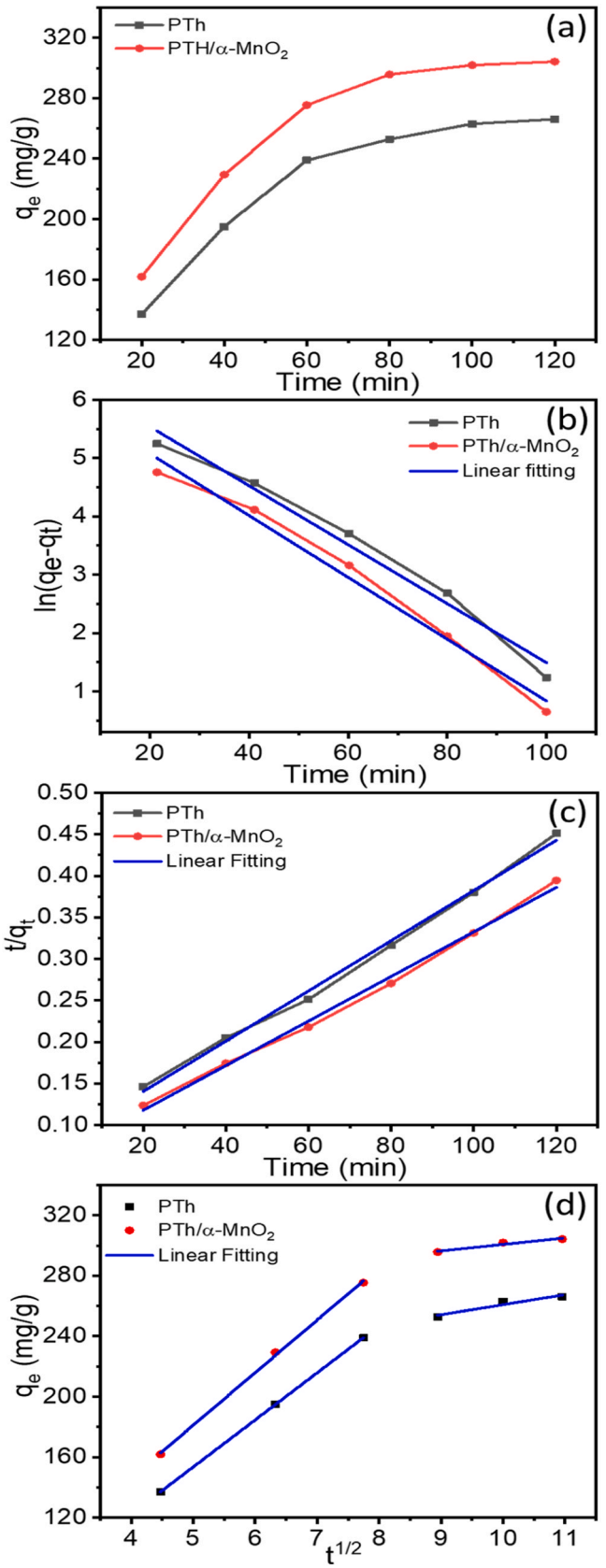

Fig. 9. (a) Time-dependence study of iodine adsorption on PTh and PTh/α-MnO_2 nanocomposite (b) Pseudo-first-order linear fitting (c) Pseudo-second-order linear fitting (d) Intraparticle diffusion linear fitting [Initial I_2 conc. 100 mg/L, dose 0.3 g/L, time 2 h, pH 4.8 and temperature 25 °C].

Table 2
Kinetic models for the iodine adsorption on PTh, and PTh/α-MnO_2 nanocomposite.

Kinetic Model	Parameters	PTh	PTh/α-MnO_2
Pseudo-first-order	q_e [mg/g]	227.36	274.45
	k_1 [minutes^{-1}]	0.04	0.0409
	R^2	0.986	0.989
Pseudo-second-order	q_e [mg/g]	261.09	312.13
	k_2 [g/(mg.minutes)]	9.12 * 10^{-5}	4.89 * 10^{-5}
	R^2	0.994	0.998
Intra-particle diffusion	k_{d1}	35.92	35.05
	c	-23.21	-11.27
	R^2	0.998	0.997
	k_{d2}	39.04	33.42
	c	-24.94	77.52
	R^2	0.949	0.930

MnO_2 to Mn_2O_3 [59]. The thermogram of PTh shows initial weight loss of 16 % in temperature range 25–150 °C due to dehydration of moisture. Moreover, a substantial weight reduction of 60 % occurred between 150 and 550 °C, attributed to the predominant connection of thiophene rings in a α−α fashion. The minimal torsion angle between these rings contributed to heightened steric resistance within the polymer chain, ultimately leading to the decomposition of the polymer backbone [36]. DSC curve shows two exothermic peak at 55 °C and 363 °C. The TGA plot PTh/α-MnO_2 nanocomposite shows first weight loss of 7 % due to removal of physically and chemically adsorbed water molecule. Furthermore, only 26 % weight loss in the temperature range of 150–550 °C, confirmed that the introduction of α-MnO_2 in the PTh, increases the thermal stability of the nanocomposites, which may be due to the strong interactions between the α-MnO_2 and PTh [60].

3.2. Adsorption experiment

3.2.1. The effect of different adsorbents and doses

The effect of different adsorbents on iodine adsorption was investigated and shown in Fig. 8a-b. The equilibrium iodine adsorption capacity for bare α-MnO_2 and bare PTh was found to be 56 mg/g and 266.08 mg/g. In contrast, the 20 % α-MnO_2 loaded PTh showed 304.21 mg/g adsorption capacity and on further increase in loading showed decreased iodine adsorption capacity, these results indicating that PTh/20 % α-MnO_2 was an efficient adsorbent for iodine removal from aqueous solution. The detailed experiments for iodine adsorption on PTh/20 % α-MnO_2 nanocomposite and PTh were performed by changing various parameters, including the time-dependent, the effect of initial iodine concentration, the effect of pH of the solution, and common ions.

In the adsorption process, the optimum dose is an important parameter, so the effect of adsorbent dosage on iodine adsorption by PTh, and PTh/α-MnO_2 nanocomposite was studied, with the dose varied between 0.1 and 0.6 g/L at a constant initial iodine concentration of 100 mg/L, pH of the iodine solution 4.8, temperature 25 °C, adsorption time 2 h, and shaker speed 250 rpm. As shown in the Fig. 8c, the number active sites for adsorption increased as the adsorbent dosage increased. However, once the dosage reached 0.3 g/L, the adsorptive capacity reached a plateau and after this, the adsorption capacity decreased due to the iodine interactions with larger empty adsorption sites. Further experiments were performed at 0.3 g/L adsorbent dose for iodine removal from the aqueous solution.

3.2.2. Kinetics model

The time-dependent studies of iodine adsorption from aqueous solution were carried out on PTh and PTh/α-MnO_2 nanocomposite. 10 mL iodine solution were withdrawn at a time interval of 20 min and the amount of I_2 was quantified by UV–vis spectrophotometer as shown in. Fig. 9a. As the reaction proceeds, active sites are occupied fast during the first 80 min then slowed down and equilibrium has been reached up to 120 min [61]. Pseudo-first-order kinetics, pseudo-second-order kinetics, and intraparticle diffusion model were utilized to examine the time-dependent study of iodine removal from an aqueous solution. Eqs. (4), (5), and (6) are their linear forms.

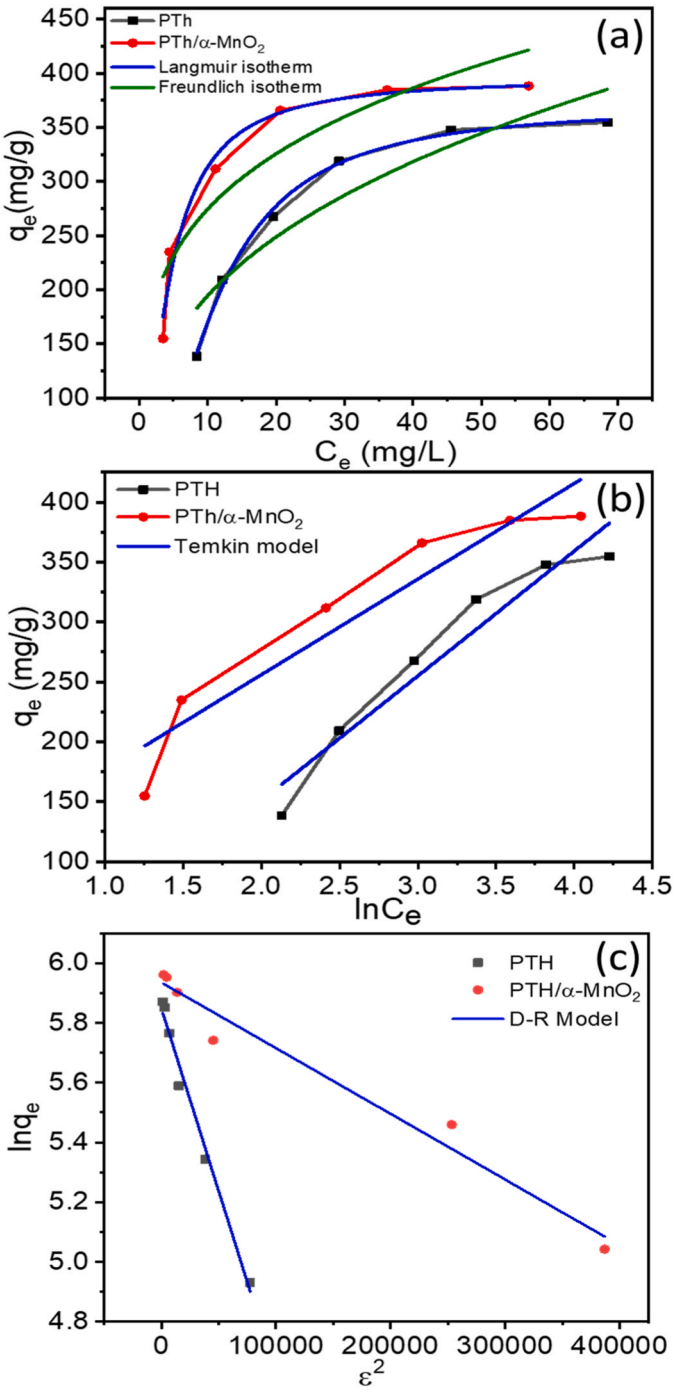

Fig. 10. (a) Langmuir and Freundlich Adsorption isotherms non linear fittings (b) Dubinin–Radushkevich (D–R) Adsorption isotherm linear fitting (c) Temkin Adsorption isotherm linear fitting for adsorption of iodine on PTh and PTH/α-MnO_2 nanocomposite [I_2 conc. 25–200 mg/L, time 2 h, dose 0.3 g/L, pH 4.8 and temperature 25 °C].

$$\ln(q_e - q_t) = \ln q_e - k_1 t \quad (4)$$

$$\frac{t}{q_t} = \frac{1}{k_2 q_e^2} + \frac{t}{q_e} \quad (5)$$

Table 3
Isotherm parameters for iodine adsorption on PTh and PTh/α-MnO_2 nanocomposite.

Model	Parameters	PTh	PTh/α-MnO_2
Langmuir	q_{max} [mg/g]	369.95	396.38
	b [L/mg]	0.0128	0.291
	R_L	0.181	0.120
	R^2	0.996	0995
Freundlich	k_F [L/mg]	85.71	155.34
	$1/n$	0.356	0.274
	R^2	0.871	0.846
Temkin	k_T	0.48	2.52
	b_T	31.05	23.99
	β	79.79	104.14
	R^2	0.992	0.995
Dubinin-Radushkevich	q_s [mg/g]	239.84	284.01
	k_D [mol^2/kJ^{-2}]	1.22 * 10^7	2.19 * 10^7
	E_{ad} [$kJmol^{-1}$]	0.202	0.151
	R^2	0.984	0.971

$$q_t = k_d t^{1/2} + c \tag{6}$$

Where q_t and q_e represent the adsorption capacity at time t and equilibrium, respectively. The rate constants for pseudo-first-order, pseudo-second-order, and intra-particle diffusion are k_1, k_2, and k_d respectively and c represents interlayer thickness. The pseudo-second-order kinetics model is more suitable, and has a higher linear correlation coefficient (R^2) compared with pseudo-first-order kinetics for PTh and PTh/α-MnO_2 nanocomposite, and obtained results are given in the Table 2, suggesting that iodine adsorption was mainly controlled by the chemical interaction process [5].

Furthermore, the intra-particle diffusion model was used to investigate the adsorption mechanism. The two linear segments were found, the first linear segment shows a relatively high linear fitting with an R^2 = 0.998 correlation coefficient due to the large amounts of active sites on the adsorbent surface, while the second linear segment is the gradual adsorption stage in PTh and PTh/α-MnO_2 nanocomposite. The intra-particle diffusion rate indicates that diffusion plays a vital role during the iodine adsorption process [62].

3.2.3. Adsorption isotherm

The effect of concentrations on iodine adsorption from an aqueous solution was examined on PTh and PTh/α-MnO_2 nanocomposite. The Langmuir isotherm, Freundlich isotherm, Temkin isotherm, and Dubinin–Radushkevich (D–R) isotherm models were fitted to experimental data to assess adsorption outcomes, shown in Fig. 10 a–d. Langmuir isotherm is represented as Eq. (7):

$$q_e = \frac{q_{max}\ k_L c_e}{(1 - k_L c_e)} \tag{7}$$

Where c_e [mg/g] and q_e [mg/g] are the concentration and adsorption capacity at equilibrium of iodine in aqueous solution, q_{max} is the maximum adsorption capacity for monolayer coverage and k_L is the Langmuir constant related to the attraction between the sorbent and the sorbate. Freundlich isotherm is represented as Eq. (8):

$$q_e = k_F (c_e)^{1/n} \tag{8}$$

Where q_e and c_e are the adsorption capacity [mg/g] and concentration [mg/L] at equilibrium, k_F and n are the Freundlich isotherm constants. The Langmuir and Freundlich isotherm models were used for the investigation of monolayer/multilayer adsorption and homogeneity/heterogeneity of solid-phase sorbents surface [63,64]. The various isotherm models were fitted, and calculated parameters are listed in Table 3.

The Langmuir isotherm correlation coefficient ($R^2 = 0.99$) was larger than the Freundlich isotherm (R^2 =0.84) for PTh/α-MnO_2 nanocomposite, showing that the adsorption of iodine was in a monolayer and takes place on the homogeneous surface of PTh, and PTh/α-MnO_2 nanocomposite. The maximum adsorption capacity (q_m) of the PTh/α-MnO_2 nanocomposite (396.38 mg/g) is larger than that of PTh (369.95 mg/g). The I_2 adsorption capacity of PTh/α-MnO_2 nanocomposite was compared to recently publish other adsorbents in the literature (Table 4).

The key feature of the Langmuir isotherm can be described in terms of a dimensionless constant, separation factor, R_L, which is defined by Eq. (9):

$$R_L = \frac{1}{1 + bc_0} \tag{9}$$

Where c_0 is the initial concentration and b is the Langmuir constant. The value of R_L reveals the kind of isotherm, if, $R_L = 0$ it will be irreversible, $0 < R_L < 1$ favorable, $R_L = 1$ linear, and $R_L > 1$ unfavorable. The value of R_L was calculated (Table 3) and lying between 0 and 1 supported favorable adsorption process [65].

Furthermore, the linear form Temkin isotherm is represented as Eq. (10):

$$q_e = \beta \ln k_T + \beta \ln c_e \tag{10}$$

$$\beta = \frac{RT}{b_T} \tag{11}$$

where R= 8.314 [$Jmol^{-1}K^{-1}$] is the gas constant, T [K] is the temperature, k_T [L/g] and β [J/mol] correspond to the binding constant, and

Table 4
Isotherm parameters for iodine adsorption on PTh, and PTh/α-MnO_2 nanocomposite.

Adsorbent	Conc [ppm]	Dose [g/L]	Temp [°C]	Time [h]	q_e [mg/g]	q_{max} [mg/g]	References
Polydopamine modified polypropylene membrane	-	-	30	2	200	221.6	[43]
Pyridine N-oxides (NTPO)	-	1.5	30	24	-	1040	[66]
Magnetite nanoparticles encapsulated in polypyrrole	100	0.04	30	3	1285	1627	[67]
MXene-PDA-Bi_6O_7 composites	20	0.2	30	6	63.65	260.06	[10]
Chitosan-MOF composite	400	1	25	1.5	363	399.68	[68]
Hydrogen-Bonded Cross-Linked Organic Framework	288	1.5	25	4	-	2100	[69]
Flowerlike $Bi_2O_{2.33}$	20	0.2	25	10	83.7	284.9	[27]
Ag-Ag_2O modified on Carbon Spheres	-	0.6	-	2		374.9	[70]
Montmorillonite- magnetite NPs	1000	0.66	35	2	38.9	322	[71]
Triptycene-based hyper crosslinked polymer	200	0.2	25	2	-	926	[72]
Bi_2O_3/LDHs	100	1	25	3	-	101.9	[73]
N-rich porous organic polymers	100	0.5	25	24	-	525.10	[74]
Conjugated microporous polymers containing thiophene units	250	0.5	25	8	184	191.62	[75]
PTh	100	0.3	25	2	266.08	369.95	our work
PTh/α-MnO_2	100	0.3	25	2	304.21	396.38	our work

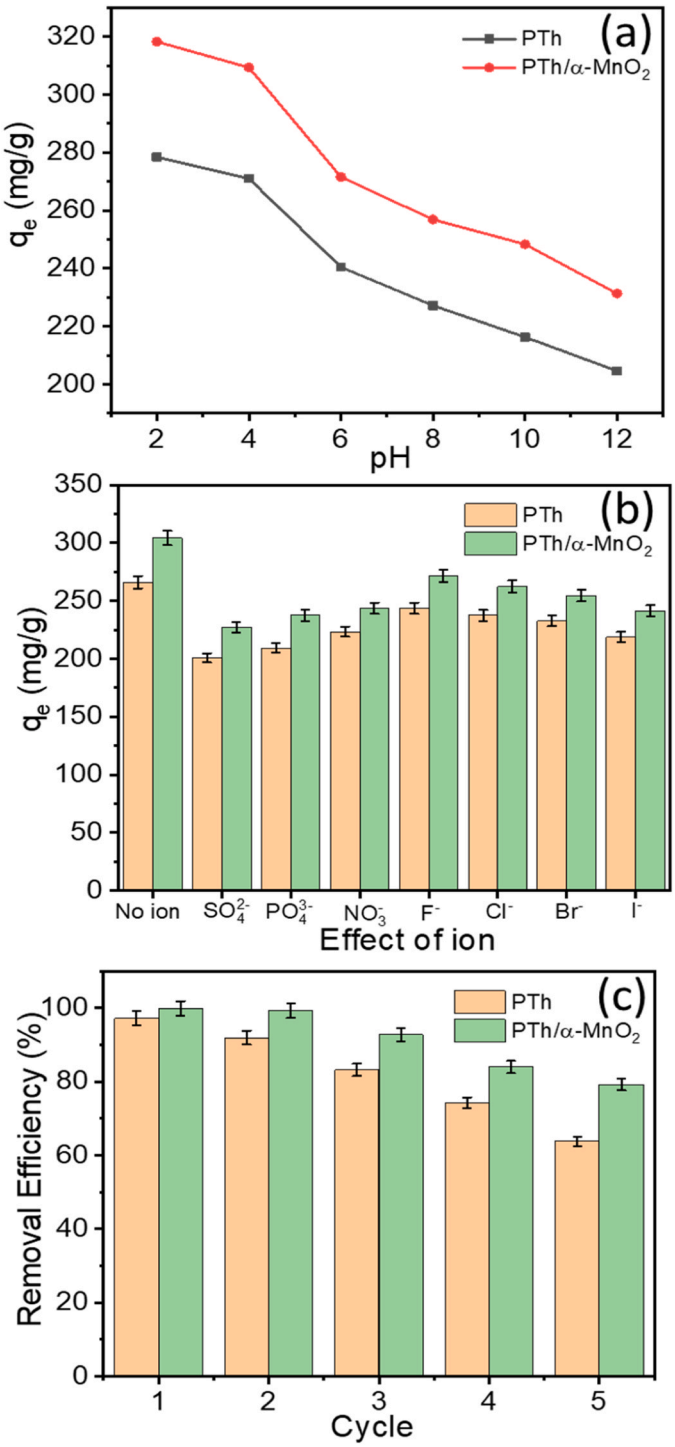

Fig. 11. (a) Effect of pH for iodine adsorption on PTh and PTh/α-MnO_2 nanocomposite (b) Effect of ions for iodine adsorption on PTh and PTh/α-MnO_2 nanocomposite (c) Recycling of the PTh and PTh/α-MnO_2 nanocomposite. (Initial iodine concentration 100 mg/L, dose 0.3 g/L, pH 2–12, temperature 25 °C, and time 2 h).

maximum binding energy was determined by plotting q_e against $\ln c_e$. According to Eq. (11), the Temkin isotherm constant b_T was calculated using β, which stands for the heat of adsorption. The positive value of the b_T showed the endothermic adsorption of iodine on the surface of PTh and PTh/α-MnO_2 nanocomposite (Table 3) [76].

Linear form Dubinin–Radushkevich (D–R) isotherm is represented as Eq. (12):

$$\ln q_e = \ln q_s - k_D \epsilon^2 \quad (12)$$

$$\epsilon = RT\ln\left[1 + \frac{1}{c_e}\right] \quad (13)$$

Where ϵ is the Polanyi potential calculated by Eq. (13), q_e [mg/g] is the adsorption capacity at saturation, k_D [mol^2kJ^{-2}] is a constant for D–R isotherm, could be calculated by plotting $\ln q_e$ against ϵ^2 using Eq. (12). E_{ad} is the mean free energy [$kJmol^{-1}$] of the adsorption process as determined by the following Eq. (14):

$$E_{ad} = \left(\frac{1}{2k_D}\right)^{1/2} \quad (14)$$

Based on the E_{ad} value adsorption was carried out through ion exchange ($8 \leq E_{ad} \geq 16$), physical ($E_{ad} < 8$ $kJmol^{-1}$), and chemical ($E_{ad} >$ 16 $kJmol^{-1}$) [77]. The slope and intercept of the plot of $\ln q_e$ versus ϵ^2 were used to determine the isotherm constants q_s and k_D, which are listed in Table 3. The observed E_{ad} values for iodine adsorption onto PTh and PTh/α-MnO_2 were 0.202 and 0.151 $kJmol^{-1}$, respectively, indicating that physical forces dominated the adsorption process [78].

3.2.4. *Effect of pH, ions, and Recyclability*

The pH of the solution is the main parameter in the adsorption process, which affects adsorption capacity and surface charge of the adsorbent (Fig. 11a) [79]. In acidic media (pH < 6), adsorbents surfaces were positively charged, attracting negatively charged iodine I_3^- via cation-anion electrostatic interaction, which increases the adsorption capacity [27]. At pH 2, adsorption capacity was found to be 278.38 and 318.03 mg/g for PTh and a PTh/α-MnO_2 nanocomposite, respectively. In the basic medium, hydroxide ions lead to a reduction in surface protonation of adsorbents and repulsion between iodine I_3^- ion and hydroxide ions, decreasing the iodine adsorption capacity [73].

Iodine adsorption from aqueous solution was investigated on PTh and PTh/α-MnO_2 nanocomposite in the presence of competing ions keeping iodine concentration 100 mg/L, salt concentration 20 mg/L, adsorbents dose 0.3 g/L, pH of the iodine solution 4.8, temperature 25 °C, adsorption time 60 min, and shaker speed 250 rpm. Fig. 11b showed that the adsorption capacity decreased in the presence of anion species due to decrease in electrostatic.

attraction between the anions and the composites, leading to fierce competition increase for active sites [73]. In the presence of halide anions (F, Cl, Br, I), adsorption capacity decreases due to intermolecular interaction between halide anions and I_2, in following order F>Cl>Br>I. Additionally adsorption capacity in presence of SO_4^{2-}, PO_4^{3-}, NO_3^- significantly degrade in order to NO_3^-> PO_4^{3-}> SO_4^{2-}. This degradation could be partly attributed to the high negative charge density of NO_3^- and basic nature of PO_4^{3-}> SO_4^{2-} salt, making hard iodine adsorption on the surfaces of PTh and PTh/α-MnO_2 nanocomposite [67]. The overall iodine adsorption capacity in the presence of anions on PTh, and PTh/α-MnO_2 nanocomposite follows the order: F^- > Cl^- > Br^- > NO_3^- > I^- > PO_4^{3-} > SO_4^{2-}.

The regeneration of adsorbents is an important process in assessing an adsorbent's potential in treatment of wastewater in large scale. 50 mg adsorbents after the I_2 adsorption were washed in 50 mL ethanol by stirring 3 h at room temperature. After this, the adsorbents were washed with distilled water and used for I_2 adsorption again. As the number of cycles increased, the percentage removal after each cycle gradually reduced in both PTh and PTh/α-MnO_2 nanocomposite, as shown in the Fig. 11c. The percentage removal after the fifth cycles, the adsorption capacity reduced from 97 % to 63 % and 99–79 % for PTh and PTh/α-MnO_2 nanocomposite, respectively. The reduced iodine adsorption capacity might be attributable to a little obstruction of active sites and adsorbent loss [62].

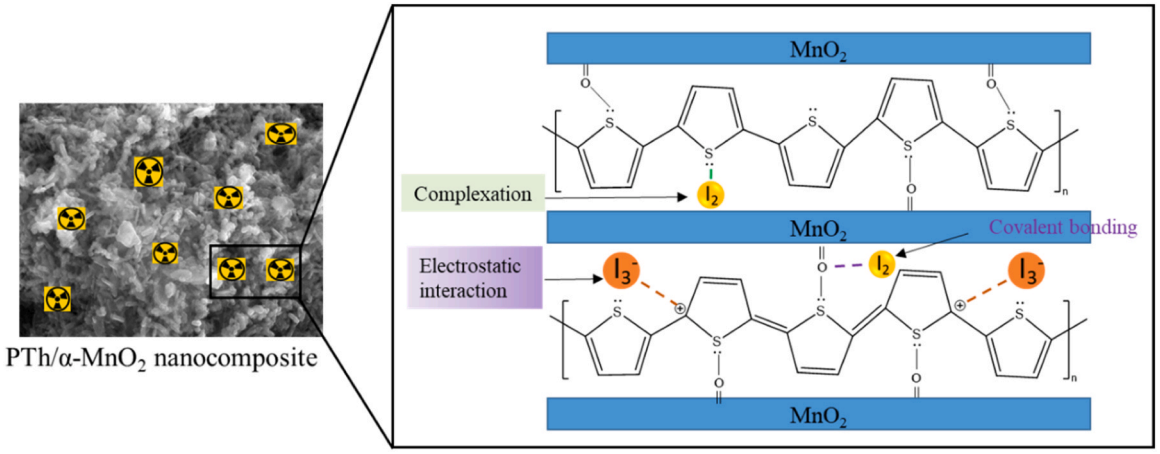

Fig. 12. Iodine adsorption mechanism onto the surface of PTh/α-MnO_2 nanocomposite.

3.2.5. *Iodine adsorption mechanism*

Iodine adsorption onto the surface of PTh, PTh/α-MnO_2 nanocomposite can be explained by electrostatic interaction and complexation, as shown in Fig. 12. Iodine in the aqueous solution mainly exist in three form, such as molecular iodine, tri-iodides ($I_2 + I^- \leftrightarrow I_3^-$), and molecular iodine in gaseous form [5]. Electrostatic interactions took place between the anionic molecules and the positively charged groups that were attached to the adsorbent surfaces. XPS spectra of S 2p in Fig. 3e confirm the presence of a polaron and a bipolaron in the PTh/α-MnO_2 nanocomposite [33,60]. The attraction between positively charged PTh and negatively charged tri-iodide accounts for electrostatic interaction [80]. Zinat Changani et al. report polypropylene membrane for the removal of iodine using polydopamine [43]. Molecular iodine is adsorbed onto PTh/α-MnO_2 through a charge transfer process, involving the donation of electron density from the lone pair orbital(s) of a sulfur atom to the antibonding molecular orbital (σ *) of I_2 [67]. This interaction results in the creation of an outer charge complex known as PTh-I_2 [81]. α-MnO_2 also plays a vital role in adsorption process due to covalent bond formation between the lone pair of the molecular iodine and manganese atom [57]. Recentaly, Nan Wang et al. have report removal of various iodine species at the Bi_2O_3@MnO_2 interface [29].

4. Conclusion

α-MnO_2, PTh, and PTh/α-MnO_2 nanocomposite were synthesized, and they showed a high I_2 adsorption capacity from aqueous solution. A TEM image reveals the formation of rod-shaped α-MnO_2 nanoparticles encapsulated in globular PTh polymeric matrix. The HRTEM image of PTh/α-MnO_2 showed lattice fringes with an interplanar distance 0.70 nm, corresponds to (211) lattice plane. The pore size of all the samples was in the range of 2–50 nm, indicating the formation of mesoporous materials. The adsorption kinetics and isotherm data were fitted well with pseudo-second-order kinetic and Langmuir adsorption isotherm model, respectively. The maximum iodine adsorption capacity was found to be 369.95 mg/g, and 396.38 mg/g on PTh, and the PTh/α-MnO_2 nanocomposite, respectively. The iodine adsorption mechanism can be explained by electrostatic interaction and complexation. After five cycles adsorption performance of PTh/α-MnO_2 nanocomposite only reduce to 20 %. The PTh/α-MnO_2 nanocomposite does have certain limitations, such as being nonmagnetic nature and experiencing a reduction in adsorption capacity after five cycle. However, despite these drawbacks, the PTh/α-MnO2 nanocomposite remains environmentally friendly and recyclable. It offers an uncomplicated and cost-effective approach for effectively adsorbing I2 from aqueous solutions.

Declaration of Competing Interest

The authors declare that they have no known competing interests.

Acknowledgement

This work was financially supported by the Department of Science and Technology, India (SERB/EMR/2016/007607).

References

[1] M.A. Bhakare, K.D. Lokhande, P.S. Dhumal, M.P. Bondarde, S. Some, Multifunctional heteroatom doped sustainable carbon nanocomposite for rapid removal of persistent organic pollutant and iodine from water, Sep. Purif. Technol. 278 (2022), 119490, https://doi.org/10.1016/j.seppur.2021.119490.
[2] S. Sun, X. Sha, J. Liang, G. Yang, X. Hu, Z. He, Rapid synthesis of polyimidazole functionalized MXene via microwave-irradiation assisted multi-component reaction and its iodine adsorption performance, J. Hazard. Mater. 420 (2021), 126580, https://doi.org/10.1016/j.jhazmat.2021.126580.
[3] A. Ahmed, A. Shah, K. Qureshi, K. Waheed, N. Irfan, W. Siddique, M. Ahmad, A. Farooq, Investigation of iodine removal efficiency in a venturi scrubber using mass transfer model for CFD, Prog. Nucl. Energy 121 (2020), 103243, https://doi.org/10.1016/j.pnucene.2020.103243.
[4] H. Jeong, D.W. Lee, S.J. Hong, J. Kim, M. Kim, J. Kim, H.S. Lee, T.H. Park, H. K. Kim, J. Il Park, J.Y. Kim, S.H. Lim, T. Hyeon, B. Han, S.E. Bae, Selective removal of radioactive iodine from water using reusable Fe@Pt adsorbents, Water Res 222 (2022), 118864, https://doi.org/10.1016/j.watres.2022.118864.
[5] R. Chen, T. Hu, Y. Li, Stable nitrogen-containing covalent organic framework as porous adsorbent for effective iodine capture from water, React. Funct. Polym. 159 (2021), 104806, https://doi.org/10.1016/j.reactfunctpolym.2020.104806.
[6] E. Yazdankish, M. Foroughi, M.H.A. Azqhandi, Capture of I131 from medical-based wastewater using the highly effective and recyclable adsorbent of g-C3N4 assembled with Mg-Co-Al-layered double hydroxide, J. Hazard. Mater. 389 (2020), 122151, https://doi.org/10.1016/j.jhazmat.2020.122151.
[7] Y.Y. Chen, S.H. Yu, Q.Z. Yao, S.Q. Fu, G.T. Zhou, One-step synthesis of Ag2O@Mg (OH)2 nanocomposite as an efficient scavenger for iodine and uranium, J. Colloid Interface Sci. 510 (2018) 280–291, https://doi.org/10.1016/j.jcis.2017.09.073.
[8] C. Zhi, B.X. Hu, W. Chang, G. Wu, Y. Dong, Q. Wang, Enrichment mechanism of fluoride and iodine in saline groundwater in the lower flood plain of the Yellow River, northern China, J. Hydrol. 621 (2023), 129529, https://doi.org/10.1016/j.jhydrol.2023.129529.
[9] Y. Guan, Y. Li, J. Zhou, T. Zhang, J. Ding, Z. Xie, L. Wang, Defect engineering of nanoscale Hf-based metal-organic frameworks for highly efficient iodine capture, Inorg. Chem. 60 (2021) 9848–9856, https://doi.org/10.1021/acs.inorgchem.1c01120.
[10] X. Sha, H. Huang, S. Sun, H. Huang, Q. Huang, Z. He, M. Liu, N. Zhou, X. Zhang, Y. Wei, Mussel-inspired preparation of MXene-PDA-Bi6O7composites for efficient adsorptive removal of iodide ions, J. Environ. Chem. Eng. 8 (2020), 104261, https://doi.org/10.1016/j.jece.2020.104261.
[11] K. Xue, C. Yang, Y. He, A review of technologies for bromide and iodide removal from water, Environ. Technol. Rev. 12 (2023) 129–148, https://doi.org/10.1080/21622515.2023.2184275.
[12] J. Li, H. Zhang, T. Xue, Q. Xiao, T. Qi, J. Chen, Z. Huang, How to recover iodine more efficiently? Extraction of triiodide, Sep. Purif. Technol. 277 (2021), 119364, https://doi.org/10.1016/j.seppur.2021.119364.
[13] X. Yu, W. Cui, F. Zhang, Y. Guo, T. Deng, Removal of iodine from the salt water used for caustic soda production by ion-exchange resin adsorption, Desalination 458 (2019) 76–83, https://doi.org/10.1016/j.desal.2019.02.006.

[14] D. Trishitman, A. Cassano, A. Basile, N.K. Rastogi, 9 - Reverse osmosis for industrial wastewater treatment, in: A. Basile, A. Cassano, N.K. Rastogi (Eds.), Curr. Trends Futur. Dev. Membr., Elsevier, 2020, pp. 207–228, https://doi.org/10.1016/B978-0-12-816777-9.00009-5.
[15] X. Long, Y.S. Chen, Q. Zheng, X.X. Xie, H. Tang, L.P. Jiang, J.T. Jiang, J.H. Qiu, Removal of iodine from aqueous solution by PVDF/ZIF-8 nanocomposite membranes, Sep. Purif. Technol. 238 (2020), 116488, https://doi.org/10.1016/j.seppur.2019.116488.
[16] K. Tokunaga, Y. Takahashi, K. Tanaka, N. Kozai, Effective removal of iodate by coprecipitation with barite: behavior and mechanism, Chemosphere 266 (2021), 129104, https://doi.org/10.1016/j.chemosphere.2020.129104.
[17] D. Li, D.I. Kaplan, K.A. Price, J.C. Seaman, K. Roberts, C. Xu, P. Lin, W. Xing, K. Schwehr, P.H. Santschi, Iodine immobilization by silver-impregnated granular activated carbon in cementitious systems, J. Environ. Radioact. 208–209 (2019), 106017, https://doi.org/10.1016/j.jenvrad.2019.106017.
[18] J. Kang, T.G. Levitskaia, S. Park, J. Kim, T. Varga, W. Um, Nanostructured MgFe and CoCr layered double hydroxides for removal and sequestration of iodine anions, Chem. Eng. J. 380 (2020), 122408, https://doi.org/10.1016/j.cej.2019.122408.
[19] M. Yadollahi, H. Hamadi, V. Nobakht, Capture of iodine in solution and vapor phases by newly synthesized and characterized encapsulated Cu2O nanoparticles into the TMU-17-NH2 MOF, J. Hazard. Mater. 399 (2020), 122872, https://doi.org/10.1016/j.jhazmat.2020.122872.
[20] H. Huang, X. Sha, Y. Cui, S. Sun, H. Huang, Z. He, M. Liu, N. Zhou, X. Zhang, Y. Wei, Highly efficient removal of iodine ions using MXene-PDA-Ag2Ox composites synthesized by mussel-inspired chemistry, J. Colloid Interface Sci. 567 (2020) 190–201, https://doi.org/10.1016/j.jcis.2020.02.015.
[21] R. Ma, F. Wang, J. Lin, H. Guo, T. Zhou, S. Liu, Z. Guo, X. Guo, An amino-decorated porous metal-organic framework for efficient C2 hydrocarbon/CH4 separation and high iodine adsorption, Microporous Mesoporous Mater. 305 (2020), 110306, https://doi.org/10.1016/j.micromeso.2020.110306.
[22] Z. Tauanov, V.J. Inglezakis, Removal of iodide from water using silver nanoparticles-impregnated synthetic zeolites, Sci. Total Environ. 682 (2019) 259–270, https://doi.org/10.1016/j.scitotenv.2019.05.106.
[23] P. Mu, H. Sun, T. Chen, W. Zhang, Z. Zhu, W. Liang, A. Li, A sponge-Like 3D-PPy monolithic material for reversible adsorption of radioactive iodine, Macromol. Mater. Eng. 302 (2017) 1–7, https://doi.org/10.1002/mame.201700156.
[24] S. Vetri, V. Lincy, S. Chen, P. Hong, A. Prasannan, Highly soluble polythiophene-based strontium-doped NiO nanocomposite for effective electrochemical detection of catechol in contaminated water, J. Mol. Liq. 334 (2021), 116490, https://doi.org/10.1016/j.molliq.2021.116490.
[25] P. Mao, L. Qi, X. Liu, Y. Liu, Y. Jiao, S. Chen, Y. Yang, Synthesis of Cu/Cu2O hydrides for enhanced removal of iodide from water, J. Hazard. Mater. 328 (2017) 21–28, https://doi.org/10.1016/j.jhazmat.2016.12.065.
[26] G. Wei, X. Shu, Z. Zhang, Q. Li, Y. Liu, X. Wang, Y. Xie, B. Li, D. Shao, X. Lu, B2O3–Bi2O3–ZnO based materials for low-sintering temperature immobilization of iodine adsorbed waste, J. Solid State Chem. 289 (2020), 121518, https://doi.org/10.1016/j.jssc.2020.121518.
[27] S. Liu, S. Kang, H. Wang, G. Wang, H. Zhao, W. Cai, Nanosheets-built flowerlike micro/nanostructured Bi2O2.33 and its highly efficient iodine removal performances, Chem. Eng. J. 289 (2016) 219–230, https://doi.org/10.1016/j.cej.2015.12.101.
[28] I.K. Jung, Y. Jo, S.C. Han, J. Il Yun, Efficient removal of iodide anion from aqueous solution with recyclable core-shell magnetic Fe3O4@Mg/Al layered double hydroxide (LDH), Sci. Total Environ. 705 (2020), 135814, https://doi.org/10.1016/j.scitotenv.2019.135814.
[29] N. Wang, R. Xiong, G. Zhang, R. Liu, X. He, S. Huang, H. Liu, J. Qu, Species transformation and removal mechanism of various iodine species at the Bi2O3@MnO2 interface, Water Res. 223 (2022), 118965, https://doi.org/10.1016/j.watres.2022.118965.
[30] J. Ma, C. Wang, W. Xi, Q. Zhao, S. Wang, M. Qiu, J. Wang, X. Wang, Removal of radionuclides from aqueous solution by manganese dioxide-based nanomaterials and mechanism research: a review, ACS EST Eng. 1 (2021) 685–705, https://doi.org/10.1021/acsestengg.0c00268.
[31] K. Namsheer, C.S. Rout, Conducting polymers: a comprehensive review on recent advances in synthesis, properties and applications, RSC Adv. 11 (2021) 5659–5697, https://doi.org/10.1039/d0ra07800j.
[32] R. Kumar, J. Travas-Sejdic, L.P. Padhye, Conducting polymers-based photocatalysis for treatment of organic contaminants in water, Chem. Eng. J. Adv. 4 (2020), 100047, https://doi.org/10.1016/j.ceja.2020.100047.
[33] Y. Wang, Y. Xie, Z. Zheng, D. Zeng, Y. Dai, Z. Zhang, X. Cao, R. Zou, Y. Liu, Surfactant-assisted adsorption of uranyl ions in aqueous solution on TiO2/polythiophene nanocomposite, Environ. Sci. Pollut. Res. 28 (2021) 37182–37194, https://doi.org/10.1007/s11356-021-12587-5.
[34] J. Chen, L. Zhang, J. Zhu, N. Wang, J. Feng, W. Yan, Adsorption of polythiophene/TiO2 composite for Zn (II), Pb (II) and Cu (II): selectivity and synergistic effect investigation, Appl. Surf. Sci. 459 (2018) 318–326, https://doi.org/10.1016/j.apsusc.2018.08.008.
[35] A. Nematollahzadeh, A. Babapoor, S. Mojtaba, A. Nuri, Nitrobenzene adsorption from aqueous solution onto polythiophene-modified magnetite nanoparticles, Mater. Chem. Phys. 262 (2021), 124266, https://doi.org/10.1016/j.matchemphys.2021.124266.
[36] X. Liu, Y. Wang, T.C. Zhang, G. Xiang, X. Wang, S. Yuan, One-pot synthesis of a magnetic TiO2/PTh/γ-Fe2O3 heterojunction nanocomposite for removing trace arsenite via simultaneous photocatalytic oxidation and adsorption, Ind. Eng. Chem. Res. 60 (2021) 528–540, https://doi.org/10.1021/acs.iecr.0c04262.
[37] D. Hussain, M.F. Siddiqui, T.A. Khan, Preparation of NiFe 2 O 4 /polythiophene nanocomposite and its enhanced adsorptive uptake of Janus green B and Fuchsin basic from aqueous solution: Isotherm and kinetics studies, Environ. Prog. Sustain. Energy 39 (2020) 1–11, https://doi.org/10.1002/ep.13371.
[38] Q. Lu, Y. Zhou, Synthesis of mesoporous polythiophene / MnO 2 nanocomposite and its enhanced pseudocapacitive properties, J. Power Sources 196 (2011) 4088–4094, https://doi.org/10.1016/j.jpowsour.2010.12.059.
[39] J. Zia, E.S. Aazam, U. Riaz, Highly efficient visible light driven photocatalytic activity of MnO2 and Polythiophene/MnO2 nanohybrids against mixed organic pollutants, J. Mol. Struct. 1207 (2020), 127790, https://doi.org/10.1016/j.molstruc.2020.127790.
[40] S. Chen, J. Chen, R. Dong, S. Chen, D. Tang, X. Lou, C. Ye, Selective adsorption towards heavy metal ions on the green synthesized polythiophene / MnO2 with a synergetic effect Selective adsorption towards heavy metal ions on the green synthesized polythiophene / MnO 2 with a synergetic effect, J. Clean. Prod. 338 (2022), 130536, https://doi.org/10.1016/j.jclepro.2022.130536.
[41] D.N. Thanh, M. Singh, P. Ulbrich, F. Štěpánek, N. Strnadová, As(V) removal from aqueous media using α-MnO2 nanorods-impregnated laterite composite adsorbents, Mater. Res. Bull. 47 (2012) 42–50, https://doi.org/10.1016/j.materresbull.2011.10.004.
[42] M. Khandani, M. Yousefi, S.S.S. Afghahi, M.M. Amini, M. Bikhof Torbati, Sr(CeNd)xFe12−2xO19/polythiophene nano-particles: structral investigation, magnetic properties and photocatalyic activity, Inorg. Chem. Commun. 121 (2020), 108214, https://doi.org/10.1016/j.inoche.2020.108214.
[43] Z. Changani, A. Razmjou, A. Taheri-Kafrani, M.E. Warkiani, M. Asadnia, Surface modification of polypropylene membrane for the removal of iodine using polydopamine chemistry, Chemosphere 249 (2020), 126079, https://doi.org/10.1016/j.chemosphere.2020.126079.
[44] T. Chhabra, A. Kumar, A. Bahuguna, V. Krishnan, Reduced graphene oxide supported MnO 2 nanorods as recyclable and e ffi cient adsorptive photocatalysts for pollutants removal, Vacuum 160 (2019) 333–346, https://doi.org/10.1016/j.vacuum.2018.11.053.
[45] V. Dinh, M. Nguyen, Q. Hung, Chemosphere Chitosan-MnO 2 nanocomposite for effective removal of Cr (VI) from aqueous solution, Chemosphere 257 (2020), 127147, https://doi.org/10.1016/j.chemosphere.2020.127147.
[46] M. Karegar, M.M. Khodaei, The modified <scp>polythiophene-Cu NPs</scp> composites for Pb(<scp>II</scp>) ions removal from aqueous solution, J. Appl. Polym. Sci. 139 (2022) 51489, https://doi.org/10.1002/app.51489.
[47] S. Mallakpour, M. Madani, Use of valine amino acid functionalized α-MnO2/chitosan bionanocomposites as potential sorbents for the removal of lead(II) ions from aqueous solution, Ind. Eng. Chem. Res. 55 (2016) 8349–8356, https://doi.org/10.1021/acs.iecr.6b02016.
[48] F.A. Harraz, M. Faisal, M. Jalalah, A.A. Almadiy, S.A. Al-Sayari, M.S. Al-Assiri, Conducting polythiophene/α-Fe2O3 nanocomposite for efficient methanol electrochemical sensor, Appl. Surf. Sci. 508 (2020), 145226, https://doi.org/10.1016/j.apsusc.2019.145226.
[49] J. Li, R. Guo, Q. Ma, L. Nengzi, X. Cheng, Efficient removal of organic contaminant via activation of potassium, Sep. Purif. Technol. 227 (2019), 115669, https://doi.org/10.1016/j.seppur.2019.06.007.
[50] Y. Li, R. Zhao, S. Chao, B. Sun, C. Wang, X. Li, Polydopamine coating assisted synthesis of MnO2 loaded inorganic/organic composite electrospun fiber adsorbent for efficient removal of Pb2+ from water, Chem. Eng. J. 344 (2018) 277–289, https://doi.org/10.1016/j.cej.2018.03.044.
[51] D. Ying, P. Hong, F. Jiali, T. Qinqin, L. Yuhui, W. Youqun, Z. Zhibin, C. Xiaohong, L. Yunhai, Biomass and Bioenergy Removal of uranium using MnO 2 / orange peel biochar composite prepared by activation and in-situ deposit in a single step, Biomass Bioenergy 142 (2020), 105772, https://doi.org/10.1016/j.biombioe.2020.105772.
[52] M.R. Chandra, T.S. Rao, S.V.N. Pammi, B. Sreedhar, Materials Science in Semiconductor Processing An enhanced visible light active rutile titania – copper / polythiophene nanohybrid material for the degradation of rhodamine B dye, Mater. Sci. Semicond. Process 30 (2015) 672–681, https://doi.org/10.1016/j.mssp.2014.09.009.
[53] A.K. Mishra, N.R. Agrawal, I. Das, Synthesis of water dispersible dendritic amino acid modified polythiophenes as highly effective adsorbent for removal of methylene blue, J. Environ. Chem. Eng. 5 (2017) 4923–4936, https://doi.org/10.1016/j.jece.2017.09.017.
[54] M. Zhang, J. Wang, Y. Zhang, M. Zhang, Y. Zhou, Simultaneous removal of NO and Hg 0 in fl ue gas over Co-Ce oxide modi fi ed rod-like MnO 2 catalyst: Promoting e ff ect of Co doping on activity and SO 2 resistance, 276, 2020. https://doi.org/10.1016/j.fuel.2020.118018.
[55] K. Shang, S. Ai, Q. Ma, T. Tang, H. Yin, H. Han, Effective photocatalytic disinfection of E. coli and S. aureus using polythiophene / MnO 2 nanocomposite photocatalyst under solar light irradiation, DES 278 (2011) 173–178, https://doi.org/10.1016/j.desal.2011.05.017.
[56] R. Bardestani, G.S. Patience, S. Kaliaguine, Experimental methods in chemical engineering: specific surface area and pore size distribution measurements—BET, BJH, and DFT, Can. J. Chem. Eng. 97 (2019) 2781–2791, https://doi.org/10.1002/cjce.23632.
[57] T.A. Abdullah, R.T. Rasheed, T. Juzsakova, N. Al-Jammal, M.A. Mallah, L. P. Cuong, A.D. Salman, E. Domokos, Z. Ali, I. Cretescu, Preparation and characterization of - MnO 2 – based nanoparticles at different annealing temperatures and their application in dye removal from water, Int. J. Environ. Sci. Technol. 18 (2021) 1499–1512, https://doi.org/10.1007/s13762-020-02956-x.
[58] V.-P. Dinh, M.-D. Nguyen, Q.H. Nguyen, T.-T.-T. Do, T.-T. Luu, A.T. Luu, T.D. Tap, T.-H. Ho, T.P. Phan, T.D. Nguyen, L.V. Tan, Chitosan-MnO2 nanocomposite for

effective removal of Cr (VI) from aqueous solution, Chemosphere 257 (2020), 127147, https://doi.org/10.1016/j.chemosphere.2020.127147.
[59] C. Almquist, M. Krekeler, L. Jiang, An investigation on the structure and catalytic activity of cryptomelane-type manganese oxide materials prepared by different synthesis routes, Chem. Eng. J. 252 (2014) 249–262, https://doi.org/10.1016/j.cej.2014.04.102.
[60] S. Iqbal, J. Shah, R.K. Kotnala, S. Ahmad, Highly efficient low cost EMI shielding by barium ferrite encapsulated polythiophene nanocomposite, J. Alloy. Compd. 779 (2019) 487–496, https://doi.org/10.1016/j.jallcom.2018.11.307.
[61] Q. Yu, X. Jiang, Z. Cheng, Y. Liao, Q. Pu, M. Duan, Millimeter-sized Bi2S3@ polyacrylonitrile hybrid beads for highly efficient iodine capture, New J. Chem. 44 (2020) 16759–16768, https://doi.org/10.1039/d0nj03229h.
[62] B. Liu, X. Ren, L. Chen, X. Ma, Q. Chen, Q. Sun, L. Zhang, P. Si, L. Ci, High efficient adsorption and storage of iodine on S, N co-doped graphene aerogel, J. Hazard. Mater. 373 (2019) 705–715, https://doi.org/10.1016/j.jhazmat.2019.04.005.
[63] L. Sun, K. Li, J. Huang, Z. Jiang, Y. Huang, H. Liu, G. Wei, F. Ge, X. Ye, Y. Zhang, A. Wu, Zhijian Wu, Facile synthesis of tri(octyl-decyl) amine-modified biomass carbonaceous aerogel for rapid adsorption and removal of iodine ions, Chem. Eng. Res. Des. 144 (2019) 228–236, https://doi.org/10.1016/j.cherd.2019.02.013.
[64] X. Li, Y. Peng, Q. Jia, Construction of hypercrosslinked polymers with dual nitrogen-enriched building blocks for efficient iodine capture, Sep. Purif. Technol. 236 (2020), 116260, https://doi.org/10.1016/j.seppur.2019.116260.
[65] M.M. Hamed, M. Holiel, Y.F. El-Aryan, Removal of selenium and iodine radionuclides from waste solutions using synthetic inorganic ion exchanger, J. Mol. Liq. 242 (2017) 722–731, https://doi.org/10.1016/j.molliq.2017.07.035.
[66] W.X. Wu, H.C. Liu, W.J. Jin, Halogen Bonding Adsorbent Pyridine N-oxides for Iodine Capture in Water, Chem. – A Eur. J. 28 (2022), e202103336, https://doi.org/10.1002/chem.202103336.
[67] D.K.L. Harijan, V. Chandra, T. Yoon, K.S. Kim, Radioactive iodine capture and storage from water using magnetite nanoparticles encapsulated in polypyrrole, J. Hazard. Mater. 344 (2018) 576–584, https://doi.org/10.1016/j.jhazmat.2017.10.065.
[68] M. El-Shahat, A.E. Abdelhamid, R.M. Abdelhameed, Capture of iodide from wastewater by effective adsorptive membrane synthesized from MIL-125-NH2 and cross-linked chitosan, Carbohydr. Polym. 231 (2020), 115742, https://doi.org/10.1016/j.carbpol.2019.115742.
[69] Y. Lin, X. Jiang, S.T. Kim, S.B. Alahakoon, X. Hou, Z. Zhang, C.M. Thompson, R. A. Smaldone, C. Ke, An elastic hydrogen-bonded cross-linked organic framework for effective iodine capture in water, J. Am. Chem. Soc. 139 (2017) 7172–7175.
[70] F. Yu, Y. Chen, Y. Wang, C. Liu, W. Ma, Enhanced removal of iodide from aqueous solution by ozonation and subsequent adsorption on Ag-Ag 2 O modified on Carbon Spheres, Appl. Surf. Sci. 427 (2018) 753–762, https://doi.org/10.1016/j.apsusc.2017.08.089.
[71] J. Jang, D.S. Lee, Magnetite nanoparticles supported on organically modified montmorillonite for adsorptive removal of iodide from aqueous solution: optimization using response surface methodology, Sci. Total Environ. 615 (2018) 549–557, https://doi.org/10.1016/j.scitotenv.2017.09.324.
[72] Q.M. Zhang, T.L. Zhai, Z. Wang, G. Cheng, H. Ma, Q.P. Zhang, Y.H. Zhao, B. Tan, C. Zhang, Hyperporous carbon from triptycene-based hypercrosslinked polymer for iodine capture, Adv. Mater. Interfaces 6 (2019) 1–6, https://doi.org/10.1002/admi.201900249.
[73] T. Zhang, X. Yue, L. Gao, F. Qiu, J. Xu, J. Rong, J. Pan, Hierarchically porous bismuth oxide/layered double hydroxide composites: preparation, characterization and iodine adsorption, J. Clean. Prod. 144 (2017) 220–227, https://doi.org/10.1016/j.jclepro.2017.01.030.
[74] X. Qian, B. Wang, Z.Q. Zhu, H.X. Sun, F. Ren, P. Mu, C. Ma, W.D. Liang, A. Li, Novel N-rich porous organic polymers with extremely high uptake for capture and reversible storage of volatile iodine, J. Hazard. Mater. 338 (2017) 224–232, https://doi.org/10.1016/j.jhazmat.2017.05.041.
[75] X. Qian, Z.Q. Zhu, H.X. Sun, F. Ren, P. Mu, W. Liang, L. Chen, A. Li, Capture and reversible storage of volatile iodine by novel conjugated microporous polymers containing thiophene units, ACS Appl. Mater. Interfaces 8 (2016) 21063–21069, https://doi.org/10.1021/acsami.6b06569.
[76] D. Zhang, S.G. Lu, X.Q. Song, J.F. Zhang, Z.M. Huo, H.T. Zhao, Synergistic and simultaneous biosorption of phenanthrene and iodine from aqueous solutions by soil indigenous bacterial biomass as a low-cost biosorbent, RSC Adv. 8 (2018) 39274–39283, https://doi.org/10.1039/c8ra07088a.
[77] S. Gupta, S.K. Ben, V. Chandra, Synthesis of titanium phosphate/polypyrrole nanocomposites for removal of methyl orange from water, Polym. Compos. 43 (2022) 9143–9157, https://doi.org/10.1002/pc.27092.
[78] F. Yu, Y. Chen, Y. Wang, C. Liu, W. Ma, Enhanced removal of iodide from aqueous solution by ozonation and subsequent adsorption on Ag-Ag 2 O modified on Carbon Spheres, Appl. Surf. Sci. 427 (2018) 753–762, https://doi.org/10.1016/j.apsusc.2017.08.089.
[79] W. Mu, X. Li, G. Liu, Q. Yu, X. Xie, H. Wei, Y. Jian, Safe disposal of radioactive iodide ions from solutions by Ag2O grafted sodium niobate nanofibers, Dalt. Trans. 45 (2016) 753–759, https://doi.org/10.1039/c5dt03458b.
[80] J. Chen, J. Zhu, N. Wang, J. Feng, W. Yan, Hydrophilic polythiophene/SiO2 composite for adsorption engineering: green synthesis in aqueous medium and its synergistic and specific adsorption for heavy metals from wastewater, Chem. Eng. J. 360 (2019) 1486–1497, https://doi.org/10.1016/j.cej.2018.10.228.
[81] S. Xiong, X. Tang, C. Pan, L. Li, J. Tang, G. Yu, Carbazole-bearing porous organic polymers with a mulberry-like morphology for efficient iodine capture, ACS Appl. Mater. Interfaces 11 (2019) 27335–27342, https://doi.org/10.1021/acsami.9b07679.

View publication stats